Origins of high ductility exhibited by an extruded magnesium alloy Mg-1.8Zn-0.2Ca: experiments and crystal plasticity modeling

Jie Wang[a,b], Gaoming Zhu[a], Leyun Wang[a,e,*], Evgenii Vasilev[b], Jun-Sang Park[c], Gang Sha[d], Xiaoqin Zeng[a,e,*], Marko Knezevic[b,*]

[a] National Engineering Research Center of Light Alloy Net Forming, Shanghai Jiao Tong University, Shanghai 200240, China

[b] Department of Mechanical Engineering, University of New Hampshire, Durham, NH 03824, USA

[c] Advanced Photon Source, Argonne National Laboratory, Lemont, IL, 60439, USA

[d] School of Materials Science and Engineering, Nanjing University of Science and Technology, Nanjing 210094, China

[e] State Key Laboratory of Metal Matrix Composites, Shanghai Jiao Tong University, Shanghai 200240, China

* Corresponding authors.

E-mail addresses: leyunwang@sjtu.edu.cn (L.Y. Wang); xqzeng@sjtu.edu.cn (X.Q. Zeng); marko.knezevic@unh.edu (M. Knezevic).

Graphical Abstract

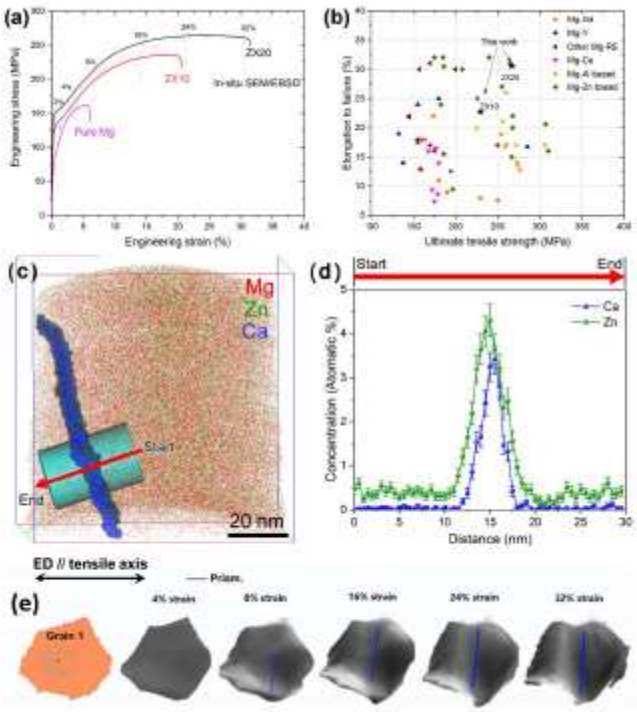

Highlights

- Highly deformable Mg-1.8Zn-0.2Ca (wt.%) alloy with ultimate tensile strength of ~265 MPa and tensile elongation of ~30% is synthesized via permanent casting and one-step hot extrusion.
- Prismatic slip is promoted in the alloy due to significantly reduced ratio of slip resistances between prismatic and basal slip systems as revealed by modeling.
- Zn and Ca solutes are found to strongly segregate at grain boundaries.
- Co-segregation of Zn and Ca makes grain boundaries stronger allowing grains to rotate without initiating cracks at grain boundaries during deformation.
- Co-segregation of Zn and Ca makes grain boundaries tougher by mediating plasticity at grain boundaries during deformation.

Abstract

Low ductility and strength are major bottlenecks against Mg alloys' wide applications.

In this work, we systematically design the composition and fabrication process for a

low-alloyed Mg-Zn-Ca alloy, showing that it can be extruded at low temperatures (~250 ℃) and high speeds (~2 mm/s). After the extrusion, this alloy exhibits a substantially weakened basal texture, relatively small grain size, very high tensile elongation (~30%), and good strength. The origin of the considerably improved ductility was studied using a combination of three-dimensional atom probe tomography (3D-APT), transmission electron microscopy (TEM), electron backscattered diffraction (EBSD) in conjunction with surface slip trace analysis, in-situ synchrotron X-ray diffraction, and elasto-plastic self-consistent (EPSC) modeling. Co-segregation of Zn and Ca atoms at a grain boundary is observed and associated with texture weakening and grain boundary mediated plasticity, both improving the ductility. While basal slip and prismatic slip are identified as the dominant deformation systems in the alloy, the ratio between their slip resistances is substantially reduced relative to pure Mg and most other Mg alloys, significantly contributing to the improved ductility of the alloy. This Mg-Zn-Ca alloy exhibiting excellent mechanical properties and low fabrication cost is a promising candidate for industrial productions.

Keywords: Mg-Zn-Ca alloy; Ductility; Deformation mechanisms; Crystal plasticity modeling; Grain boundary mediated plasticity

1. Introduction

As a lightweight metal, Mg has received extensive attention in the last two decades because of its potential to replace Al alloys and steels for structural applications[1,2]. However, widespread usage of Mg and its alloys remains limited mainly due to their poor room-temperature ductility and the resultant high cost of thermomechanical processing at elevated temperatures [3–5]. The low ductility of Mg and alloys has been associated with relatively strong texture formed during thermomechanical processing and to the difficulty to activate other than the easy basal slip systems during plastic deformation at room temperature [6–10].

The addition of rare earth (RE) elements, such as Y, Gd, and Ce, into Mg, has been proved to be an effective solution to make ductile Mg alloys[11–17]. The improved ductility of RE-containing Mg alloys is ascribed to the altered texture and the non-basal slip system activities. It has been widely observed that Mg-RE alloys exhibit a weakened texture due to the appearance of a new texture component, called “RE texture”, during thermomechanical processing and subsequent annealing[18,19]. RE textures normally reduce the anisotropy and asymmetry of Mg alloys, which consequently allow these alloys to be deformed more homogeneously with improved formability. Furthermore, first-principle computations indicate that RE elements can reduce the critical resolved shears stress (CRSS) ratio between non-basal slip and basal slip, thus allowing more non-basal slip to be activated[20–22]. The increased activity

of pyramidal <*c*+*a*> slip in Mg-RE alloys is believed to be the origin of its high ductility[23].

For economic reasons, it is crucial to find alloying additions that are not strategic metals that have similar beneficial properties as RE elements. Fortunately, researchers recently found that the addition of Zn and Ca together to Mg results in a weakened texture after recrystallization[24,25]. Furthermore, Mg-Zn-Ca ternary alloy sheets and extrusions often show excellent ductility[26–32]. Mg-Zn and Mg-Ca binary alloys were studied using a variety of methods to elucidate the effects of the solutes on deformation behavior. Blake et al. reported that activated prismatic slip improves the ductility of Mg-Zn solid solutions (single crystal) because of the softening effect of Zn solutes on prismatic slip[33]. Using atomistic simulations, Jang and Lee found that Zn can activate <*c*+*a*> slip by reducing CRSS anisotropy among slip systems that improves ductility[34]. Zhu et al. identified an increased activity of pyramidal <*a*> slip in Mg-Ca alloy based on a statistical slip trace analysis, which was used to explain the improved ductility induced by Ca addition[35]. Other researchers using molecular dynamics (MD) or density functional theory (DFT) concluded that either Ca atoms have higher dislocation binding energy and solid solution strengthening on basal <*a*> slip than on <*c*+*a*> slip or Ca could promote basal-to-prismatic cross-slip in Mg-Ca alloy[36–38]. Note that the Mg-Zn and Mg-Ca binary alloys often show a strong basal texture, which is not the case for Mg-Zn-Ca ternary alloys. The overall understanding of the role of Zn and Ca solutes on the deformation mechanism of Mg alloys remains unclear.

The discrepancy of the interpretations from different researchers can be caused by different investigating methods. Until now, most studies on identifying the deformation mechanism of Mg alloys were conducted using post-deformation samples by transmission electron microscope (TEM) in a few grains, from which it is difficult to yield a full picture of deformation behavior. Electron backscattered diffraction (EBSD)-assisted slip trace analysis[35,39], on the other hand, provides direct and statistically sound evidence of the active deformation mechanisms and has recently been proven to be key to solving several remaining controversies regarding the plasticity of Mg alloys. Nevertheless, the EBSD-based analysis still has its limitation because slip lines can only be observed on the surface of the sample; those subsurface slip activity cannot be characterized. On top of that, the free surface leads to stress relaxation, which may influence the accuracy of the statistical results.

The high-brilliance synchrotron source, enabling in-situ high-energy X-ray to penetrate the bulk material, is a powerful tool for studying the deformation characteristics of many metallic materials in situ[40–46]. Specifically, the lattice strain can be measured from the shift in diffraction peak position during deformation. The texture change can also be obtained from the evolution of diffraction peak intensity. The plastic flow characteristics, such as the evolution of dislocation density, can also be investigated through the line-broadening analysis. But still, some key material parameters, like CRSS values, are difficult to obtain for polycrystalline materials purely from

experiments[47,48]; a modeling framework needs to be employed to deduce these material parameters.

In this work, we designed and synthesized a highly ductile Mg alloy with a small amount of Zn and Ca concentrations. Considering the low cost and relatively simple manufacturing process, this new Mg-Zn-Ca alloy has great potential for mass productions. The main objective of this work is to study the origins of high ductility exhibited by the designed Mg-Zn-Ca alloy. To give a comprehensive understanding, various experimental methods, including in-situ SEM/EBSD and in-situ synchrotron X-ray diffraction, combined with crystal plasticity modeling were used to reveal the deformation mechanisms. The alloying effects on the deformation behavior unveiled in this study can be guidelines for the development of similar Mg alloys in future works.

2. Experimental methods

2.1 Material synthesis

The design of this wrought Mg-Zn-Ca alloy follows the following guidelines. First, the concentration of Ca should be below its maximum solubility (0.71 wt.%) to avoid the precipitation of Mg_2Ca intermetallic compound that reduces the formability[49]; Second, the concentration of Zn is incrementally increased to provide more solute strengthening (solubility limit of Zn in Mg is 6.2 wt.%); Third, the extrusion

temperature is kept relatively low to minimize grain growth and thus enhance the strength; Eventually, an Mg-1.8Zn-0.2Ca (wt.%) alloy (denoted as ZX20) was optimized and successfully extruded. Another Mg-0.9Zn-0.1Ca (wt.%) alloy (denoted as ZX10) and pure Mg extruded bars were also fabricated for the comparison purpose. The ZX10 and ZX20 alloys were made from pure Mg, pure Zn, and Mg-20 wt.% Ca master alloy in an electric resistance furnace under the protective gas consisting of CO_2 (99 vol.%) and SF_6 (1 vol.%). The melt was poured into a cylindrical steel mold preheated to 200 ^{o}C and then naturally cooled in air. The actual chemical composition of the cast billets was determined by an inductively coupled plasma atomic emission spectroscopy (ICP-AES) analyzer (Perkin-Elmer, Plasma 400). The cast billets were machined to cylindrical samples with 60 mm in diameter and 70 mm in height, followed by the homogenization at 400 ^{o}C for 12 h. One-step direct extrusion was carried out at 250 ^{o}C and 2 mm/s to produce round bars of 14 mm in diameter, which corresponds to an extrusion ratio of ~18:1.

2.2 Microstructural characterization and mechanical tests

The initial and post-deformation microstructures of the alloys were characterized by optical microscopy (OM, Zeiss Axio observer) and transmission electron microscopy (TEM, JEOL-ARM200).

Dog-bone tensile specimens with a gauge dimension of 18.0 mm (Length) × 4.8 mm (Width) × 1.4 mm (Thickness) were machined from the extruded alloys for standard tension tests. Cylindrical specimens with a diameter of 5 mm and a height of 7.5 mm were used for compression tests. The loading axes in tension tests are parallel to the extrusion direction while the compression tests were conducted with loading axes of 0°, 45°, and 90° along extrusion direction. The tension and compression tests were conducted with crosshead speeds of 0.5 and 0.2 mm/min, respectively, which result in a nominal strain rate of ~5×10^{-4} s^{-1} in both tests.

The three-dimensional atom probe tomography (3D-APT) sample was prepared by mechanically grinding a piece of the ZX20 alloy into a 0.5 mm × 0.5 mm × 10 mm rod. This rod was further electro-polished into a needle by a two-stage electro-polishing procedure. The first stage used a solution of 25% perchloric acid (70%) in glacial acetic acid at 20 V-DC, and the second stage used an electrolyte of 2% perchloric acid in 2-butoxyethanol and a potential of 20–30 V-DC. The 3D-APT experiment uses a Cameca LEAP 3000 Atom Probe (USA). The measurement was conducted under a specimen temperature of 20 K and an ultrahigh vacuum (-1.0×10^{-11} Torr). Field evaporation was induced by voltage pulsing, with a voltage pulse fraction of 0.2 and a pulse rate of 200 kHz. A target evaporation rate of 2 ions per 1000 pulses was used. The raw data was reconstructed using the IVAS 3.6.6 software and established reconstruction protocols.

2.3 In-situ SEM/EBSD

A dog-bone tensile specimen was machined from an extrusion bar with a gauge of 11.0 mm (Length) × 4.0 mm (Width) × 1.4 mm (Thickness). The length of the gauge is parallel to the extrusion direction, which would also be the tensile loading direction. One top surface of the specimen was prepared by mechanical polishing using an OPS (oxide polishing suspension) lubricant for SEM and EBSD measurements, and then mounted in a MICROTEST 200N (Deben, UK) module placed in a Zeiss Gemini SEM equipped with an EBSD system (Oxford Instrument, UK). The tensile test was conducted with a crosshead speed of 0.1 mm/min, which is equivalent to a strain rate of 1.5×10^{-4} s^{-1}. The crosshead displacement and instantaneous load were recorded during the test for estimating the instant strain and stress. The test was intermitted at the tensile strains of 0%, 1%, 2%, 4%, 8%, 16%, 24%, and 32% to allow EBSD data acquisition and secondary electron (SE) imaging for the same surface area. Since the large lattice distortion and lots of dislocations were produced during plastic deformation, EBSD acquisition became difficult after 16% strain, but SE images can still be captured beyond this strain. EBSD scans were conducted at an accelerating voltage of 20 kV with a step size of 0.4 μm. The EBSD data was analyzed using TSL OIM™ software (EDAX Inc., USA). EBSD-based slip trace analysis was performed to explore the deformation mechanisms for those grains that generated surface slip lines. The observed slip lines in a given grain are the intersection lines between the slip plane and the sample surface. With the grain orientation information obtained by EBSD, one could compute all theoretical possible slip lines associated with different slip systems.

After comparing the computational result with the observed slip lines in SEM, we can conclude the activated slip system in the given grain.

2.4 In-situ synchrotron X-ray diffraction

The in-situ high-energy X-ray diffraction (HEXRD) experiments were conducted at beamline 1-ID-E of the Advanced Photon Source at Argonne National Laboratory in the USA. The experiment setup is illustrated and described in detail in Ref. [41]. The tensile tests were carried out on an MTS 858 servo-hydraulic load frame under uniaxial tension up to failure with a strain rate of 1×10^{-4} s^{-1}. While the specimen was under continuous tensile deformation, a monochromatic X-ray illuminated the gauge center in transmissive geometry, and HEXRD patterns were recorded by detectors.

The X-ray energy was 71.68 KeV (wavelength 0.01730 nm). The size of the incident beam was 150 μm × 150 μm. The HYDRA detector array at the APS 1-ID-E endstation was used for this work[50]. In the HYDRA array, GE3 and GE4 detectors are nominally in the loading direction and transverse direction, respectively. The X-ray detector calibration was performed with a CeO_2 NIST standard (SRM 674b). The sample to detector distance was nominally 2635 mm, which led to a 2θ coverage of 10° on the X-ray detectors, and more than 9 Debye-Scherrer rings, denoted hereon as {hkil}s, were recorded. The 1D profiles were obtained by integrating over ± 7.5° azimuthal angle of the diffraction patterns in GE3 (marked by the solid lines in Fig. A1(a)) in the direction

nominally parallel to the tensile loading axis (marked by the dotted lines in Fig. A1(a)). The same was done for the patterns recorded by GE4 for the direction nominally perpendicular to the loading axis (transverse direction, TD). The 1D diffraction profiles then fitted using pseudo-Voigt functions along the two directions to obtain the integrated intensity, position, and width (represented by full-width at half maximum or FWHM) of each peak of interest. During deformation, the lattice strain of each {hkil} peak from a particular detector is calculated using $\varepsilon_{\mathrm{hkil}}(\sigma) = \frac{d_{\mathrm{hkil}}(\sigma) - d_{\mathrm{hkil}}(0)}{d_{\mathrm{hkil}}(0)}$, where $d_{\mathrm{hkil}}(0)$ is the d-spacing of the {hkil} before the tensile test and $d_{\mathrm{hkl}}(\sigma)$ is the d-spacing of the {hkil} when the specimen was under macroscopic stress σ.

For peak broadening analysis, it was assumed that the broadening is homogeneous in the entire azimuthal range (i.e. no directional preference) and the transverse direction covered by GE4 was used. The instrument contribution to the peak broadening (B) was quantified using a CeO_2 standard sample and was subtracted from the measured FWHM to get the actual sample broadening using $B^2_{\mathrm{sample}} = B^2_{\mathrm{measured}} - B^2_{\mathrm{instrument}}$.

3. Material model

The deformation behavior of ZX10 and ZX20 Mg alloys fabricated in this work is modeled using an elasto-plastic self-consistent (EPSC) material model. In EPSC, a polycrystalline aggregate is represented by ellipsoidal grains with each grain numerically imbedded as an elasto-plastic inclusion within a homogenous effective

medium (HEM), which is the response of the polycrystal. Each grain has its crystal lattice orientation and weight. In the modeling here, the texture is represented using 1000 weighted crystal orientations. The strength of the interaction between inclusion and HEM can be adjusted by a parameter M_{eff} [51,52]. The particular version of EPSC adapted here for these alloys incorporates a dislocation density-based law for the evolution of slip resistance and considers deformation twinning as an operating deformation mechanism[53]. The present work uses these recent advances to interpret the behavior of studied alloys. In what follows, the hardening law is briefly summarized.

The law was originally formulated for metals with the hexagonal structure in Ref. [54] and advanced for various aspects in subsequent works[55–63]. The slip resistance per slip mode α (basal, prismatic, pyramidal), $\tau_{\mathrm{c}}^{\alpha}$, consists of a non-evolving term, τ_{0}^{α}, which represents the friction stress embedding the Peierls stress and the initial dislocation density population and the evolution terms, $\tau_{0,\mathrm{HP}}^{s}$, which is the Hall-Petch-like barrier term dependent on the initial grain size and twins, $\tau_{\mathrm{forest}}^{\mathrm{s}}$, which is the forest term dependent on the stored dislocation density, and $\tau_{\mathrm{deb}}^{\alpha}$, which is the debris term dependent on the ordered dislocations. The relation is

$$\tau_{\mathrm{c}}^{\mathrm{s}} = \tau_{0}^{\alpha} + \tau_{0,\mathrm{HP}}^{\mathrm{s}} + \tau_{\mathrm{forest}}^{\mathrm{s}} + \tau_{\mathrm{deb}}^{\alpha}, \tag{1}$$

with

$$\tau_{0,\mathrm{HP}}^{\alpha} = \mu^{\alpha} H P^{\alpha} \sqrt{\frac{b^{\alpha}}{d_{\mathrm{g}}}}, \tag{2a}$$

$$\tau_{\mathrm{forest}}^{\mathrm{s}} = b^{\alpha} \chi \mu^{\alpha}(T) \sqrt{\rho_{\mathrm{tot}}^{\mathrm{s}} + \sum_{\mathrm{s}'} L^{\mathrm{ss}'} \rho_{\mathrm{tot}}^{\mathrm{s}}}, \tag{2b}$$

$$\tau_{\mathrm{deb}}^{\alpha} = 0.086\mu^{\alpha}b^{\alpha}\sqrt{\rho_{\mathrm{deb}}}\log\left(\frac{1}{b^{\alpha}\sqrt{\rho_{\mathrm{deb}}}}\right). \quad (2c)$$

In the above equations, χ is a dislocation interaction constant taken as 0.9[64], $\rho_{\mathrm{tot}}^{\mathrm{s}}$ is the total density of forest dislocations per slip system, *s*, μ^{α} is the shear modulus with a value for Mg of 15.5 GPa, b^{α} is magnitude of the Burgers vector, $L^{\mathrm{ss}'}$ is a matrix representing latent hardening estimated to be 1 for coplanar and 0.5 for the latent slip systems interactions and, finally, ρ_{deb} is the population of debris density. The Hall–Petch-like barrier effect contributes to hardening by grain subdivision due to the existence of twins in individual grains. With twins existing in grains, the barrier effect term is modeled using[59]

$$\tau_{\mathrm{HP}}^{\mathrm{s}} = \frac{f^{\mathrm{PTS}} - f^{\mathrm{PTS},0}}{f^{\mathrm{PTS,max}} - f^{\mathrm{PTS},0}}\mu^{\alpha}\mathrm{HP}^{\alpha}\sqrt{\frac{b^{\alpha}}{d_{\mathrm{mfp}}^{\mathrm{s}}}}, \quad (3)$$

where $d_{\mathrm{mfp}}^{\mathrm{s}}$ represents the mean-free-path of dislocations estimated using $d_{\mathrm{mfp}}^{\mathrm{s}} = \frac{(1-f^{\mathrm{PTS}})d_{\mathrm{c}}}{\sin(\alpha)}$. Here, α is the angle between the predominant twin system (PTS) plane in case multiple twins exist in a given grain and the slip plane, $d_{\mathrm{c}} = \frac{d_{\mathrm{g}}}{n^{\mathrm{lamellas}}}$ is the separation between lamellas as the ratio between the grain size, d_{g}, and the number of lamella per grain, n^{lamellas}, which is taken to be 5. The barrier factor, $\frac{f^{\mathrm{PTS}} - f^{\mathrm{PTS},0}}{f^{\mathrm{PTS,max}} - f^{\mathrm{PTS},0}}$ includes $f^{\mathrm{PTS,max}}$ and $f^{\mathrm{PTS},0}$ representing the maximum and the minimum volume fractions that twins can take. $f^{\mathrm{PTS,max}}$ is set to 0.95, while $f^{\mathrm{PTS},0}$ is set to 0.05. f^{PTS} is the volume fraction of the PTS system.

To complete the theory, we now turn attention to defining the evolution of dislocation densities. The total dislocation density is

$$\rho_{\mathrm{tot}}^{\mathrm{s}} = \rho_{\mathrm{for}}^{\mathrm{s}} + \rho_{\mathrm{rev}}^{\mathrm{s}^{+}} + \rho_{\mathrm{rev}}^{\mathrm{s}^{-}}, \quad (4)$$

where $\rho_{\mathrm{rev}}^{\mathrm{s}^+}$ and $\rho_{\mathrm{rev}}^{\mathrm{s}^-}$ are the reversible dislocation populations for the s^+ and s^- directions and $\rho_{\mathrm{for}}^{\mathrm{s}}$ is the forward density. The split facilitates modeling of strain path sensitive deformation, which is beyond the scope of the present paper. As a result, the law governing the evolution with shear strain is[65–67]

(If $\mathrm{d}\gamma^{\mathrm{s}^+} > 0$)

$$\frac{\partial \rho_{\mathrm{for}}^{\mathrm{s}}}{\partial \gamma^{\mathrm{s}}} = (1-p)k_1^{\alpha}\sqrt{\sum_{s\prime} g^{\mathrm{ss}'}\ \rho_{\mathrm{tot}}^{\mathrm{s}'}} - k_2^{\alpha}\rho_{\mathrm{for}}^{\mathrm{s}}, \tag{5a}$$

$$\frac{\partial \rho_{\mathrm{rev}}^{\mathrm{s}^+}}{\partial \gamma^{\mathrm{s}}} = pk_1^{\alpha}\sqrt{\sum_{s\prime} g^{\mathrm{ss}'}\ \rho_{\mathrm{tot}}^{\mathrm{s}'}} - k_2^{\alpha}\rho_{\mathrm{rev}}^{\mathrm{s}^+}, \tag{6a}$$

$$\frac{\partial \rho_{\mathrm{rev}}^{\mathrm{s}^-}}{\partial \gamma^{\mathrm{s}}} = -k_1^{\alpha}\sqrt{\sum_{\mathrm{s}'} g^{\mathrm{ss}'}\ \rho_{\mathrm{tot}}^{\mathrm{s}'}}\left(\frac{\rho_{\mathrm{rev}}^{\mathrm{s}^-}}{\rho_0^{\mathrm{s}}}\right)^m, \tag{7a}$$

(If $\mathrm{d}\gamma^{\mathrm{s}^-} > 0$)

$$\frac{\partial \rho_{\mathrm{for}}^{\mathrm{s}}}{\partial \gamma^{s}} = (1-p)k_1^{\alpha}\sqrt{\sum_{s\prime} g^{ss\prime}\rho_{tot}^{s\prime}} - k_2^{\alpha}\rho_{for}^{s}, \tag{5b}$$

$$\frac{\partial \rho_{\mathrm{rev}}^{\mathrm{s}^+}}{\partial \gamma^{\mathrm{s}}} = -k_1^{\alpha}\sqrt{\sum_{s\prime} g^{\mathrm{ss}'}\ \rho_{\mathrm{tot}}^{\mathrm{s}'}}\left(\frac{\rho_{\mathrm{rev}}^{\mathrm{s}^+}}{\rho_0^{\mathrm{s}}}\right)^m, \tag{6b}$$

$$\frac{\partial \rho_{rev}^{s^-}}{\partial \gamma^{s}} = pk_1^{\alpha}\sqrt{\sum_{s\prime} g^{\mathrm{ss}'}\ \rho_{\mathrm{tot}}^{\mathrm{s}'}} - k_2^{\alpha}\rho_{\mathrm{rev}}^{\mathrm{s}^-}. \tag{7b}$$

The initial conditions are $\rho_{\mathrm{for}}^{\mathrm{s}}(\gamma^{\mathrm{s}}=0) = 2.5\times10^{12}\ m^{-2}$, $\rho_{\mathrm{rev}}^{\mathrm{s}^+}(\gamma^{\mathrm{s}}=0) = 0$ and $\rho_{\mathrm{rev}}^{\mathrm{s}^-}(\gamma^{\mathrm{s}}=0) = 0$. In the above equations, k_1^{α} is a fitting material parameter responsible for the rate of generation and k_2^{α} is responsible for removal (dynamic recovery) of statistically stored dislocations[54]. p is a reversibility constant ranging from 0 to 1 but here set to 1. $g^{\mathrm{ss}'}$ is an interaction matrix taken as the identity matrix. m is a constant taken to be 0.5 and represents the rate of dislocation recombination [68]. ρ_0^{s} is the density at the reversal of the path for the system s. The k_2^{α} is calculated using

$$\frac{k_2^{\alpha}}{k_1^{\alpha}} = \frac{\chi b^{\alpha}}{g^{\alpha}}\left(1 - \frac{k_{\mathrm{B}}T}{D^{\alpha}(b^{\alpha})^3}\ln\left(\frac{\dot{\varepsilon}}{\dot{\varepsilon}_0}\right)\right). \tag{8}$$

where k_B is the Boltzmann constant, $\dot{\varepsilon}_0$ is a reference strain rate of 10^7, g^α is the activation energy, and D^α is the drag stress. The density of debris dislocations is evolved using

$$\sum_s \frac{\partial \rho_{\text{deb}}}{\partial \gamma^s} = \sum_s q^\alpha b^\alpha \sqrt{\rho_{\text{deb}}}\, k_2 \rho_{\text{tot}}^s, \tag{9}$$

where q^α is the dislocation recovery rate fitting constant. This constant separates the portion of dislocations accumulated as debris from the annihilated population.

The twinning model available in EPSC is the composite-grain (CG) formulation[69]. Twinning shear is modeled by means of the pseudo-slip model[70–73]. As the accumulated shear reaches a threshold of 0.05, the twinned domain is reoriented. The twinned domain is further modeled as a separate ellipsoid, while the volume is transmitted from the parent to the twinned domain with accommodated shear according to

$$\Delta f^t = \frac{\Delta \gamma^t}{S}, \tag{10}$$

where Δf^t is the twin volume fraction increment, $\Delta \gamma^t$ is the twin system, *t*, shearing in the grain, and *S* is the characteristic twin shear. The resistance to twin is

$$\tau_c^t = \tau_0^\beta + \tau_{\text{HP}}^t + \tau_{\text{slip}}^\beta, \tag{11}$$

with, τ_0^β as the initial value per mode, β, τ_{HP}^t is the barrier term, and τ_{slip}^β as the hardening term due to slip-twin interactions. The barrier term is formulated per system using

$$\tau_{\text{HP}}^t = \text{HP}^\beta \sqrt{\frac{1}{a_{\text{mfp}}^t}}, \tag{12}$$

where d^{t}_{mfp} is the mean-free-path. The hardening due to the interactions is defined using

$$\tau^{\beta}_{\mathrm{slip}} = \mu^{\beta} \sum_{\mathrm{s}} C^{\alpha\beta} b^{\beta} b^{\alpha} \rho^{s}_{\mathrm{tot}}, \tag{13}$$

with b^{β} as the Burgers vector and $C^{\alpha\beta}$ is the fitting hardening matrix.

4. Results

4.1 Initial microstructures and mechanical properties

The starting microstructures of the two designed alloys were characterized. Fig. 1 shows the representative micrographs of both alloys. The as-cast alloys display a coarse grain structure. There is a small amount of second phase, with black contrast in the optical micrographs, in the as-cast alloys. After heat treatment and extrusion, both alloys exhibit a fully recrystallized microstructure with equiaxed grains. Only the Mg phase was identified from the synchrotron X-ray diffraction result, as shown in Fig. A1, indicating that alloying elements mainly exist as the form of solid solution. The as-extruded ZX20 alloy with an average grain size of 6.5 μm shows a more uniform grain size distribution, which is of interest, as will be discussed shortly.

Chemical compositions and their distribution were further analyzed in an extruded ZX20 sample using 3D-APT. This technique provides a three-dimensional mapping of the distributions of both Zn and Ca atoms in the sample, as shown in Fig. 2. The presence of a grain boundary is confirmed by examining the crystallographic information obtained by APT. Fig. 2(a) shows the Mg atom density maps for successive slices of the sample volume along the analysis direction, demonstrating that two different crystal pole information in this area separated by a grain boundary. Apparently, co-segregation of Zn and Ca occurred at the grain boundary, as shown in Fig. 2(b). A line profile crossing the grain boundary shows the concentration of Ca and Zn along the red arrow (Fig. 2(c)). This line profile is obtained from a cylinder that is normal to the grain boundary, the cylindrical volume with a height of 30 nm and a diameter of 20 nm is highlighted in pale blue as shown in Fig. 2(c). Along this line, the concentrations of Zn and Ca atom are ~4.3 at% and ~3.5 at% at the grain boundary (Fig. 2(d)), which are 5.5 times and 27.5 times of their nominal concentrations in the grain interior. The co-segregation zone is about 9 nm around the grain boundary. This kind of solute segregation could influence the plastic deformation of Mg alloy, which is further analyzed in the discussion part.

The texture of the as-extruded alloys was measured by EBSD. Fig. 3 shows the EBSD map of the ZX20 alloy (a), ZX10 alloy (b), and pure Mg (c). The pole figures show that the ZX20 alloy possesses a profoundly weak texture with a strength of ~2.8 mrd compared to ZX10 of 4.8 mrd and pure Mg of 7.5 mrd under the same extrusion

condition. The texture weakening phenomenon was not observed either in Mg-Zn or Mg-Ca binary alloys, but only in Mg-Zn-Ca ternary alloys[27]. Thus, it can be concluded that combined Zn and Ca addition have a texture weakening effect on Mg, similar to RE elements.

Fig. 4(a) shows the stress-strain curves of those alloys from standard tension tests, with the tensile axis being parallel to the extrusion direction (ED). The ZX20 alloy shows much higher ductility (ε_f~30%) than the ZX10 alloy (ε_f~21%) as well as pure Mg (ε_f~6%). The tension curve obtained from in-situ SEM/EBSD test for ZX20 alloy was also plotted in Fig. 4(a). A pronounced elastic limit is observed upon reloading after each pause during the in-situ SEM/EBSD measurement. This behavior correlates with a solid solution strengthening mechanism due to solute-dislocation interactions. The so-called dynamic strain aging effect was first observed by Cottrell in iron[74]. Fig. 4(b) compares the tensile properties of the ZX20 and ZX10 alloys with other Mg alloys in the literature. The ZX20 alloy shows an outstanding balance of strength and ductility, its elongation to failure is greater than most RE-containing Mg alloys.

4.2 Deformation microstructure by in-situ SEM/EBSD

EBSD-based slip trace analysis was performed to analyze the deformation mechanisms. Fig. 5(a) shows an EBSD map of a deformed ZX20 alloy at 4% of tensile strain. It can be seen that twinning is absent in the majority of grains. Fig. 5(b) shows the result of

slip trace analysis from the same area as (a). At 4% strain, most of the slip lines belong to basal slip. Non-basal slip, such as prismatic and pyramidal <*a*>, were also occasionally identified in a few grains. A total of 211 out of 798 grains developed slip lines on the surface of the sample after 4% strain, and basal slip accounts for more than 90% of those slip lines. From the grain orientations highlighted in the EBSD map (Fig. 5(a)), we can see that most grains have their *c*-axis away from both ED and TD, indicating they are favored for activating basal slip. Given that basal slip has the lowest slip resistance among all slip modes, most of the grains in this alloy would be deformed by basal slip. Grain 1 shown in Fig. 5(c) did not develop surface slip lines until after 8% strain. The slip lines developed afterward belong to prismatic slip. Statistical slip trace analysis is useful to determine the slip activities at early deformation. However, it may not be suitable to accurately analyze slip activities at higher strain levels because slip lines formed at different strains may overlap.

Grain orientation rotation can provide additional insights into the deformation mechanism in the absence of surface slip lines. The in-situ EBSD data gives us the grain orientation information at each deformation step. The grain orientation rotation was defined as the angular difference between the crystal orientations at smaller and larger strains for each grain. The orientation rotation in 798 grains during the first loading step (0%-1% strain), in 749 grains during the second loading step (1%-2% strain), and in 746 grains during the third loading step (2%-4% strain) were calculated from the in-situ EBSD data and presented in Fig. 6(a-c) with respect to grain size measured by

EBSD. Fig. 6(d) shows the average amount of grain orientation rotation during different strain intervals. From the grain orientation rotation, we can also compute the *c*-axis tilt value. According to the dislocation theory[76], when a crystal is deformed by dislocation slip, the crystal orientation will gradually rotate around an axis that is perpendicular to both the slip plane normal and the slip Burgers vector. For those grains deformed by basal slip, their *c*-axis tilt would be the same as the overall grain orientation rotation. At early strains, the average *c*-axis tilt is very close to the average orientation rotation, indicating the dominance of basal slip. At higher strains, the average orientation rotation became significantly larger than the average *c*-axis tilt, suggesting that non-basal slip modes became more active in later deformation.

It is also found that the amount of grain orientation rotation is influenced by the grain size. As indicated by the dotted lines in Fig. 6(a-c), grains with smaller sizes tend to have larger orientation rotation. The dynamics of the grains are coupled because the two sides of any grain boundary at all times must adjoin and be in stress equilibrium. To facilitate this process, the grains have to change shapes in different ways, and their crystallographic orientations must rotate with respect to each other[77]. Dislocation slip induced grain rotation need to overcome the restraint from the adjacent grain boundaries, the grains with smaller size have a larger specific surface area, which is beneficial to accommodate the whole intragranular deformation. Likewise, the center of larger grains is more difficult to rotate compared to the areas close to grain boundaries, thus reducing the average orientation rotation for the whole grain.

4.3 In-situ X-ray diffraction

The EBSD-based analysis is confined to examine the deformation mechanisms in surface grains, which may not fully represent the bulk material behavior. In-situ synchrotron X-ray, capable of penetrating the whole bulk sample, is a desirable tool to complement the study of deformation mechanism.

Fig. 7 depicts the peak intensity evolution for {10-10}, {10-11}, {10-12}, {11-20}, and {10-13} as a function of applied engineering strain. For each peak, integrated intensity along the tension direction (recorded by GE3) was used. While there have been works by[78,79] show that crystal length scale stresses are not identical to the applied macroscopic stress particularly for materials with a higher level of elastic anisotropy, we take the traditional analysis approach as the sample could not be rotated with respect to the incident x-rays. For ZX10 alloy, the intensity of {10-10} was continuously increasing through the entire tension test, while the intensity of {11-20}, {10-12}, and {10-13} show a decreasing trend. According to the experimental setup, {10-12} and {10-13} diffraction peaks represent grains with a large Schmid factor for the basal slip. When the basal slip is activated, the *c*-axes of those grains would move away from the axial (tension) direction towards the transverse direction, decreasing the intensity of {10-12} and {10-13} while increasing the intensity of both {10-10} and {11-20}. On the contrary, the intensity of {11-20} shows a decreasing trend. This is likely due to the

activation of prismatic slip which transforms the {11-20} oriented grains to {10-10} oriented grains. In general, the peak intensity evolution of ZX20 alloy shows a similar behavior as ZX10. Two subtle differences were observed between the two alloys. First, the change in peak intensity for ZX20 was slower than ZX10. Second, after about 18% strain, the peak intensity in ZX20 became stable. This implies a change in the deformation mechanism, which will be discussed more later.

For peak broadening analysis, data obtained from the transverse direction (recorded in GE4) was used. Fig. 8(a, b) shows the evolution of full-width half-maximum (FWHM) values of six reflections, {10-10}, {0002}, {10-11}, {10-12}, {11-20} and {10-13} as a function of engineering strain. In general, the FWHM values increase rapidly at the beginning of deformation, but the increase became slower in later deformation. Two factors are contributing to the peak broadening: the size broadening related to the shrinkage of coherent scattering volume and the strain broadening related to lattice distortions[42]. Williamson-Hall (W-H) analysis was performed to separate the size and strain broadening contributions. The method is a multiple peak method that is used to separate size and strain contributions. The method works by fitting straight lines to plots of the integral breadth of different peaks, against the reciprocal of the lattice spacing, the gradient and the intercept are used to represent the strain broadening and the size broadening. More details about the Williamson-Hall analysis can be found in references[80–82]. According to the diffraction theory, the strain broadening increases with the diffraction vector length g_{hkl} ($g_{hkl} = 1/d_{hkl}$, d_{hkl} is the d-spacing of the {hkl}

plane) while the size broadening is independent of the g_{hkl}[83]. The slope of this linear relationship is proportional to the square root of the mobile dislocation density ($\sqrt{\rho}$), and the intercept is inversely proportional to the coherent scattering domain size D by the Scherrer equation ($\beta = {}^{0.9\lambda}/_{D}$, where β is the intercept and λ is the wavelength). The W-H slope and *y*-intercept values obtained from the W-H analysis for ZX10 and ZX20 are plotted against engineering strains in Fig. 8(c, d). The W-H slopes (dislocation density) of both alloys rapidly increased in the initial stage and then plateaued at higher strain.

4.4 Modeling results

To determine the slip resistance and the relative activities of deformation modes, EPSC modeling was performed. Multiple stress-strain curves were used to calibrate the model parameters. Fig. 9 compares the simulated and measured flow curves under different loading conditions, alongside with the deformation mode activity. All deformation responses for each alloy were calculated using the same set of material parameters, which is given in Table 1. The model captures these constitutive responses for both alloys. The modeling results support the findings of in-situ EBSD and X-ray diffraction analysis that basal and prismatic slip are two dominant deformation modes for the investigated alloys in ED-tension.

As another validation metric, texture evolution obtained from the model predictions and the experiment measurements was compared. Fig. 10 presents side-by-side the measured and predicted texture evolution for ZX20 alloy tested in tension along with ED. Although the texture shows a less prominent change because of the inactivity of twinning, it still can be seen that the calculated evolution trend is consistent with the measured texture. First, the {0001} fiber texture intensified with increasing strain. This change is derived from the activation of basal slip. Second, the maximum of {10-10} and {11-20} poles re-aligned with increasing strain, which is particularly obvious from inverse pole figure evolution as presented in Fig. A2. This is the result of prismatic slip.

We further compared the elastic lattice strains predicted by the model with the measured values from in-situ X-ray diffraction. Fig. 11 shows the lattice strain evolution of the {10-10}, {10-11}, {10-12}, {11-20}, {10-13}, {20-20}, {11-22}, and {20-21} reflections. In general, lattice strains show a rapid increase upon yielding followed by a slow increase rate with the increasing of the plastic strain. Overall, the simulated results agree well with the experimental measurement. The discrepancy is most obvious for {10-11}, {10-12}, {10-13}, and {11-22} reflections. The sudden drop of lattice strain upon the yield point was caused by the strain aging phenomenon [84]. Because the interaction between solutes and dislocations is not explicitly considered in EPSC, the model is unable to reproduce the drop of lattice strain in those reflections. Note that those reflections correspond to grains that are easy to activate basal slip. One implication is that the solutes tend to segregate at <*a*> dislocations on basal planes. The

simulated results, in terms of the lattice strain values and the texture intensity, are slightly higher than the experimental ones. Since the model does not include any sub-granular deformation, the grain boundary involved plastic deformation, as we revealed in this alloy will be discussed more later, could also be responsible for the overall over-prediction by the model.

In summary, the EPSC model and the associated material parameters achieved excellent prediction of mechanical response, texture evolution, and lattice strain evolution for the two alloys, especially in the early stage of deformation. The discrepancy between the measurement and prediction is caused by the grain boundary involved plasticity, which will be discussed more in the next section.

5. Discussion

The designed Mg-1.8Zn-0.2Ca (wt.%**)** extrusion alloy featured in low-alloyed non-RE addition, simple manufacturing process, high work-hardening rate, and very high elongation to failure. The following sections discuss the origin of the excellent mechanical properties in this new alloy.

5.1 Solute effect on the slip behavior in Mg

While basal slip dominated the early deformation stage due to the weak texture of ZX20 alloy, prismatic slip became very active in later deformation according to both the measured grain orientation rotation and EPSC simulation. Akhtar and Teghtsoonian[85] have reported that the CRSS for the prismatic slip in Mg single crystals decreases with an increase of Zn concentration. Stanford et al. [86]reported that 1 wt.% of Zn can reduce the CRSS ratio between prismatic slip and basal slip ($CRSS_{prismatic}/CRSS_{basal}$) from 8.0 to 5.0 in polycrystalline Mg with a grain size of 110 μm. Recent experimental and computational studies suggest that dilute Ca is also favorable for the prismatic slip to be activated in Mg. Therefore, the enhanced prismatic slip in this Mg-Zn-Ca alloy can be attributed to the joint effects of Zn and Ca solutes. But still, this cannot fully explain the excellent ductility in this alloy, since both twinning and <*c*+*a*> slip, which are critical to accommodate the *c*-axis deformation[87], were identified as inactive in this alloy. Grain boundary, therefore, was believed to play an important role in governing the plastic deformation of this alloy.

5.2 Co-segregation of Zn and Ca at grain boundaries

Co-segregation of Zn and Ca atoms at grain boundary is a key feature in this alloy. Somekawa et al. recently showed that Y or Ca atoms segregated to grain boundaries can stimulate the nucleation of non-basal dislocations[88,89]. Note that either Ca or Zn alone has a low tendency of grain boundary segregation compared with Mg-Zn-Ca

alloys. The improved ductility of Mg-Zn-Ca relative to Mg-Zn or Mg-Ca binary alloys[24,34] is attributed in part to the effects of the observed co-segregation.

The weak extrusion texture can reduce the anisotropy and asymmetry of Mg alloys, which consequently promotes more homogeneous deformation with improved ductility. Solute segregation at grain boundaries was reported as responsible for weak texture in certain Mg alloys[24,25]. In general, the strong basal texture in Mg alloys forms due to the preferential activities of basal slip and twinning during extrusion, and this strong basal texture usually retains after extrusion due to the preferential growth of recrystallized grains with specific orientations. In contrast, a hypothesis exists that solute atoms segregated to grain boundaries reduce the grain boundary mobility during recrystallization by reducing grain boundary energy and enhancing the solute drag effect, from which uniform recrystallized grains with randomized orientations tended to grow. This notion was used to explain the weak texture that occurred in RE-containing Mg alloys as well as Mg-Zn-Ca alloy[18,24]. Here we found that grain boundary facilitated some plastic deformation mediated behavior due to the strong segregation of Zn and Ca atoms to grain boundaries. The grain boundary related plastic deformation found in this work provides another explanation for the weak texture in the extruded Mg-Zn-Ca alloy, as discussed in the next section.

5.3 Grain boundary mediated plasticity

Since the model only considers intragranular deformation and grain-to-grain interactions in an averaged sense (i.e. grain-HEM), the over-estimation of lattice strains and texture evolution suggests that some intergranular plasticity may be occurring. Another indicator for grain boundary mediated plasticity (GBMP) is the intensity of diffraction peaks being stable after about a strain of 18%, which signifies that the dislocation-induced texture change is on the wane. A possible explanation is that after 18% strain, GBMP is increasingly occurring. GBMP is more general than grain boundary sliding (GBS) observed in nanocrystalline metals or at elevated temperatures. To confirm GBMP, a ZX20 sample was polished and tested in a scanning electron microscope to different strain levels, as shown in Fig. 12. Apart from the equiaxed grains being elongated along the tensile axis, motion along the grain boundaries were observed. Such GBMP becomes prevailing, particularly in the later stage of deformation.

It is generally accepted that solute segregation makes grain boundaries stronger through the dragging effect of solute atoms[90,91]. Besides, the co-segregated Zn and Ca atoms could make grain boundary tougher. To this end, atomic radius of the Ca atom is larger than Mg, whereas the atomic radius of Zn is smaller. The presence of a Zn atom at GBs releases a compression strain, while the presence of a Ca atom at GB causes relaxation of an extension strain. When the material under plastic deformation, dislocations pile up at grain boundaries. Strain localizations at grain boundaries are relaxed with Zn and

Ca atoms working together at defect sites. The smaller Zn and the larger Ca atoms have more freedom to choose their appropriate sites of defects to coordinate the distortion at grain boundaries, by which cracks are suppressed to initiate and propagate. The role of Zn and Ca solutes in mediating the plasticity processes at grain boundaries was verified by a TEM examination, as shown in Fig. 13. Elemental maps for a grain boundary in a post-deformation sample show existence of only larger Ca atoms, while smaller Zn atoms dissolved into the Mg matrix. Besides, the width of the grain boundary in this post-deformation sample is about 16 nm compared with about 9 nm prior to deformation. The width of grain boundary was estimated from the segregation zones from APT result in Fig. 2 and TEM result in Fig. 13, respectively. The GBMP behavior revealed in this work provides a novel insight into the rationalization of the improved ductility and weak texture in Mg-Zn-Ca alloys.

GBMP and GBS have been observed in pure Mg when the grain size is ~1.3 μm[6]. While the ZX20 alloy has a grain size of 6.5 μm, the co-segregation of Zn and Ca enhances GBMP and makes the GBS less reliant on grain size. Atomistic simulations can provide further understanding about the role of solute atoms on the mobility of grain boundaries.

6. Conclusions

In this work, we designed and fabricated a low-alloyed RE-free Mg-Ca-Zn alloy that shows high elongation of ~30% and strength of 265 MPa. Detailed experiments and simulations performed for the alloy reveal that cooperative action of Zn and Ca solutes enhances activity of prismatic slip relative to other slip modes. It is also found that Ca and Zn tend to co-segregate at grain boundaries, and this co-segregation leads to texture weakening and grain boundary mediated plasticity (GBMP). Activation of non-basal slip and weak texture facilitate more homogeneously deformation, and GBMP provides an extra degree of freedom improving ductility in the late deformation stages. These three effects together make this alloy highly ductile. Because this alloy has excellent formability, it can be extruded at relatively low temperatures to obtain a fine-grain microstructure (grain size ~6.5 μm). As a result, the strength is also enhanced.

Declaration of interests

☒ The authors declare that they have no known competing financial interests or personal relationships that could have appeared to influence the work reported in this paper.

Acknowledgements

We thank Jian Wang at University of Nebraska-Lincoln for valuable discussions on EBSD data analysis. This work has been financially supported by the National Key Research and Development Program of China (No. 2016YFB0701203) and the National Natural Science Foundation of China (Nos. 51631006, 51671127 and 51825101). L.W. is sponsored by the Youth Cheung Kong Scholars Program and the Shanghai Rising-Star Program. M.K. and E.V. would like to acknowledge the support

provided by the U.S. National Science Foundation (No. OIA-1757371). Use of the Advanced Photon Source was supported by the United States Department of Energy, Office of Science, Office of Basic Energy Sciences (No. DE-AC02-06CH11357).

References

[1] T.M. Pollock, Science 328 (2010) 986 – 987.

[2] J. Wang, J. Zhang, X. Zong, C. Xu, Z. You, K. Nie, Mater. Sci. Eng. A 648 (2015) 37–40.

[3] M. Lentz, M. Risse, N. Schaefer, W. Reimers, I.J. Beyerlein, Nat. Commun. 7 (2016) 11068.

[4] T.T.T. Trang, J.H. Zhang, J.H. Kim, A. Zargaran, J.H. Hwang, B.-C. Suh, N.J. Kim, Nat. Commun. 9 (2018) 2522.

[5] B.-C. Suh, M.-S. Shim, K.S. Shin, N.J. Kim, Scr. Mater. 84–85 (2014) 1–6.

[6] Z. Zeng, J.-F. Nie, S.-W. Xu, C. H. J. Davies, N. Birbilis, Nat. Commun. 8 (2017) 972.

[7] S. Sandlöbes, M. Friák, S. Korte-Kerzel, Z. Pei, J. Neugebauer, D. Raabe, Sci. Rep. 7 (2017) 10458.

[8] B.-C. Suh, J.H. Kim, J.H. Bae, J.H. Hwang, M.-S. Shim, N.J. Kim, Acta Mater. 124 (2017) 268–279.

[9] G. Zhu, L. Wang, J. Wang, J. Wang, J.-S. Park, X. Zeng, Acta Mater. 200 (2020) 236–245.

[10] Q. Dong, Z. Luo, H. Zhu, L. Wang, T. Ying, Z. Jin, D. Li, W. Ding, X. Zeng, J. Mater. Sci. Technol. 34 (2018) 1773–1780.

[11] A. Imandoust, C.D. Barrett, T. Al-Samman, K.A. Inal, H. El Kadiri, J. Mater. Sci. 52 (2017) 1–29.

[12] R.K. Mishra, A.K. Gupta, P.R. Rao, A.K. Sachdev, A.M. Kumar, A.A. Luo, in: S.N. Mathaudhu, A.A. Luo, N.R. Neelameggham, E.A. Nyberg, W.H. Sillekens (Eds.), Springer International Publishing, Cham, 2016, pp. 363–368.

[13] S. Sandlöbes, Z. Pei, M. Friák, L.-F. Zhu, F. Wang, S. Zaefferer, D. Raabe, J. Neugebauer, Acta Mater. 70 (2014) 92–104.

[14] L. Wang, Z. Huang, H. Wang, A. Maldar, S. Yi, J.-S. Park, P. Kenesei, E. Lilleodden, X. Zeng, Acta Mater. 155 (2018) 138–152.

[15] A. Kula, X. Jia, R.K. Mishra, M. Niewczas, Metall. Mater. Trans. B 47 (2016) 3333–3342.

[16] W. Li, L. Wang, B. Zhou, C. Liu, X. Zeng, J. Mater. Sci. Technol. 35 (2019) 2200–2206.

[17] A. Maldar, L. Wang, G. Zhu, X. Zeng, J. Magnes. Alloy 8 (2020) 210–218.

[18] D. Guan, X. Liu, J. Gao, L. Ma, B.P. Wynne, W.M. Rainforth, Sci. Rep. 9 (2019) 7152.

[19] D. Guan, W.M. Rainforth, J. Gao, L. Ma, B. Wynne, Acta Mater. 145 (2018) 399–412.

[20] T. Tsuru, D.C. Chrzan, Sci. Rep. 5 (2015) 8793.

[21] A. Tehranchi, B. Yin, W.A. Curtin, Acta Mater. 151 (2018) 56–66.

[22] Z. Wu, R. Ahmad, B. Yin, S. Sandlöbes, W.A. Curtin, Science 359 (2018) 447 – 452.

[23] S. Sandlöbes, S. Zaefferer, I. Schestakow, S. Yi, R. Gonzalez-Martinez, Acta Mater. 59 (2011) 429–439.

[24] Z.R. Zeng, Y.M. Zhu, S.W. Xu, M.Z. Bian, C.H.J. Davies, N. Birbilis, J.F. Nie, Acta Mater. 105 (2016) 479–494.

[25] D. Guan, X. Liu, J. Gao, L. Ma, B. Wynne, W.M. Rainforth, J. Alloys Compd. 774 (2019) 556–564.

[26] L. Geng, B.P. Zhang, A.B. Li, C.C. Dong, Mater. Lett. 63 (2009) 557–559.

[27] Z.R. Zeng, M.Z. Bian, S.W. Xu, C.H.J. Davies, N. Birbilis, J.F. Nie, Mater. Sci. Eng. A 674 (2016) 459–471.

[28] S.W. Xu, K. Oh-ishi, H. Sunohara, S. Kamado, Mater. Sci. Eng. A 558 (2012) 356–365.

[29] L.B. Tong, M.Y. Zheng, L.R. Cheng, S. Kamado, H.J. Zhang, Mater. Sci. Eng. A 569 (2013) 48–53.

[30] J. Hofstetter, S. Rüedi, I. Baumgartner, H. Kilian, B. Mingler, E. Povoden-Karadeniz, S. Pogatscher, P.J. Uggowitzer, J.F. Löffler, Acta Mater. 98 (2015) 423–432.

[31] M.G. Jiang, C. Xu, T. Nakata, H. Yan, R.S. Chen, S. Kamado, J. Alloys Compd. 668 (2016) 13–21.

[32] H. Pan, Y. Ren, H. Fu, H. Zhao, L. Wang, X. Meng, G. Qin, J. Alloys Compd. 663 (2016) 321–331.

[33] A.H. Blake, C.H. Cáceres, Mater. Sci. Eng. A 483–484 (2008) 161–163.

[34] H.-S. Jang, B.-J. Lee, Scr. Mater. 160 (2019) 39–43.

[35] G. Zhu, L. Wang, H. Zhou, J. Wang, Y. Shen, P. Tu, H. Zhu, W. Liu, P. Jin, X. Zeng, Int. J. Plast. 120 (2019) 164–179.

[36] J.A. Yasi, L.G. Hector, D.R. Trinkle, Acta Mater. 58 (2010) 5704–5713.

[37] J.A. Yasi, L.G. Hector, D.R. Trinkle, Acta Mater. 60 (2012) 2350–2358.

[38] K.-H. Kim, J.H. Hwang, H.-S. Jang, J.B. Jeon, N.J. Kim, B.-J. Lee, Mater. Sci. Eng. A 715 (2018) 266–275.

[39] C.M. Cepeda-Jiménez, J.M. Molina-Aldareguia, M.T. Pérez-Prado, JOM 68 (2016) 116–126.

[40] N. Jia, Z.H. Cong, X. Sun, S. Cheng, Z.H. Nie, Y. Ren, P.K. Liaw, Y.D. Wang, Acta Mater. 57 (2009) 3965–3977.

[41] D. Zhang, L. Wang, H. Zhang, A. Maldar, G. Zhu, W. Chen, J.-S. Park, J. Wang, X. Zeng, Acta Mater. 189 (2020) 93–104.

[42] L. Wang, M. Li, J. Almer, Acta Mater. 62 (2014) 239–249.

[43] M. Lentz, M. Klaus, I.J. Beyerlein, M. Zecevic, W. Reimers, M. Knezevic, Acta Mater. 86 (2015) 254–268.

[44] F. Zhang, L.E. Levine, A.J. Allen, M.R. Stoudt, G. Lindwall, E.A. Lass, M.E. Williams, Y. Idell, C.E. Campbell, Acta Mater. 152 (2018) 200–214.

[45] K. Sofinowski, M. Šmíd, S. van Petegem, S. Rahimi, T. Connolley, H. van Swygenhoven, Acta Mater. 181 (2019) 87–98.

[46] J. Wang, L. Wang, G. Zhu, B. Zhou, T. Ying, X. Zhang, Q. Huang, Y. Shen, X. Zeng, H. Jiang, Metall. Mater. Trans. A Phys. Metall. Mater. Sci. 49 (2018) 5382–5392.

[47] P.R. Dawson, D.E. Boyce, J.-S. Park, E. Wielewski, M.P. Miller, Acta Mater. 144 (2018) 92–106.

[48] E. Wielewski, D.E. Boyce, J.-S. Park, M.P. Miller, P.R. Dawson, Acta Mater. 126 (2017) 469–480.

[49] Z. Zeng, N. Stanford, C.H.J. Davies, J.-F. Nie, N. Birbilis, Int. Mater. Rev. 64 (2019) 27–62.

[50] J.-S. Park, X. Zhang, H. Sharma, P. Kenesei, D. Hoelzer, M. Li, J. Almer, J. Mater. Res. 30 (2015) 1380–1391.

[51] D.J. Savage, I.J. Beyerlein, N.A. Mara, S.C. Vogel, R.J. McCabe, M. Knezevic, Int. J. Plast. 125 (2020) 1–26.

[52] C.N. Tomé, Model. Simul. Mater. Sci. Eng. 7 (1999) 723–738.

[53] T.J. Barrett, R.J. McCabe, D.W. Brown, B. Clausen, S.C. Vogel, M. Knezevic, J. Mech. Phys. Solids 138 (2020) 103924.

[54] I.J. Beyerlein, C.N. Tomé, Int. J. Plast. 24 (2008) 867–895.

[55] M. Ardeljan, I.J. Beyerlein, M. Knezevic, J. Mech. Phys. Solids 66 (2014) 16–31.

[56] M. Ardeljan, M. Knezevic, T. Nizolek, I.J. Beyerlein, N.A. Mara, T.M. Pollock, Int. J. Plast. 74 (2015) 35–57.

[57] M. Ardeljan, D.J. Savage, A. Kumar, I.J. Beyerlein, M. Knezevic, Acta Mater. 115 (2016) 189–203.

[58] A. Eghtesad, M. Knezevic, J. Mech. Phys. Solids 134 (2020) 103750.

[59] M. Knezevic, M. Zecevic, I.J. Beyerlein, J.F. Bingert, R.J. McCabe, Acta Mater. 88 (2015) 55–73.

[60] M. Knezevic, M. Zecevic, I.J. Beyerlein, R.A. Lebensohn, Comput. Methods Appl. Mech. Eng. 308 (2016) 468–482.

[61] M. Zecevic, M. Knezevic, Comput. Methods Appl. Mech. Eng. 341 (2018) 888–916.

[62] M. Zecevic, Y.P. Korkolis, T. Kuwabara, M. Knezevic, J. Mech. Phys. Solids 96 (2016) 65–87.

[63] M. Zecevic, M. V Upadhyay, E. Polatidis, T. Panzner, H. Van Swygenhoven, M. Knezevic, Acta Mater. 166 (2019) 386–401.

[64] F.F. Lavrentev, Mater. Sci. Eng. 46 (1980) 191–208.

[65] M. Khadyko, S. Dumoulin, G. Cailletaud, O.S. Hopperstad, Int. J. Plast. 76 (2016) 51–74.

[66] K. Kitayama, C.N. Tomé, E.F. Rauch, J.J. Gracio, F. Barlat, Int. J. Plast. 46 (2013) 54–69.

[67] H. Mecking, U.F. Kocks, Acta Metall. 29 (1981) 1865–1875.

[68] W. Wen, M. Borodachenkova, C.N. Tomé, G. Vincze, E.F. Rauch, F. Barlat, J.J. Grácio, Int. J. Plast. 73 (2015) 171–183.

[69] G. Proust, C.N. Tomé, G.C. Kaschner, Acta Mater. 55 (2007) 2137–2148.

[70] M. Knezevic, M.R. Daymond, I.J. Beyerlein, Scr. Mater. 121 (2016) 84–88.

[71] M. Knezevic, R.A. Lebensohn, O. Cazacu, B. Revil-Baudard, G. Proust, S.C. Vogel, M.E. Nixon, Mater. Sci. Eng. A 564 (2013) 116–126.

[72] M. Knezevic, A. Levinson, R. Harris, R.K. Mishra, R.D. Doherty, S.R. Kalidindi, Acta Mater. 58 (2010) 6230–6242.

[73] P.V. Houtte, Acta Metall. 26 (1978) 591–604.

[74] A.H. Cottrell, B.A. Bilby, Proc. Phys. Soc. Sect. A 62 (1949) 49–62.

[75] R.K. Sabat, A.P. Brahme, R.K. Mishra, K. Inal, S. Suwas, Acta Mater. 161 (2018) 246–257.

[76] M.A. Meyers, K.K. Chawla, Mechanical Behavior of Materials, Cambridge University Press, 2008.

[77] L. Margulies, G. Winther, H.F. Poulsen, Science 291 (2001) 2392 LP – 2394.

[78] Y.D. Wang, X.-L. Wang, A.D. Stoica, J.W. Richardson, R. Lin Peng, J. Appl. Crystallogr. 36 (2003) 14–22.

[79] J. V Bernier, J.-S. Park, A.L. Pilchak, M.G. Glavicic, M.P. Miller, Metall. Mater. Trans. A 39 (2008) 3120–3133.

[80] P. Scardi, M. Leoni, R. Delhez, J. Appl. Crystallogr. 37 (2004) 381–390.

[81] V. Soleimanian, S.R. Aghdaee, Powder Diffr. 23 (2008) 41–51.

[82] D. Balzar, N. Audebrand, M.R. Daymond, A. Fitch, A. Hewat, J.I. Langford, A. Le Bail, D. Louër, O. Masson, C.N. McCowan, J. Appl. Crystallogr. 37 (2004) 911–924.

[83] T. Ungár, A. Borbély, Appl. Phys. Lett. 69 (1996) 3173–3175.

[84] M.Z. Bian, T.T. Sasaki, T. Nakata, Y. Yoshida, N. Kawabe, S. Kamado, K. Hono, Acta Mater. 158 (2018) 278–288.

[85] A. Akhtar, E. Teghtsoonian, Acta Metall. 17 (1969) 1351–1356.

[86] N. Stanford, M.R. Barnett, Int. J. Plast. 47 (2013) 165–181.

[87] B. Song, Q. Yang, T. Zhou, L. Chai, N. Guo, T. Liu, S. Guo, R. Xin, J. Mater. Sci. Technol. 35 (2019) 2269–2282.

[88] H. Somekawa, D.A. Basha, A. Singh, T. Tsuru, M. Yamaguchi, Mater. Trans. (2020) MT-M2020040.

[89] H. Somekawa, D.A. Basha, A. Singh, Materialia 8 (2019) 100466.

[90] W.T. Sun, X.G. Qiao, M.Y. Zheng, C. Xu, S. Kamado, X.J. Zhao, H.W. Chen, N. Gao, M.J. Starink, Acta Mater. 151 (2018) 260–270.

[91] J. Hu, Y.N. Shi, X. Sauvage, G. Sha, K. Lu, Science 355 (2017) 1292–1296.

Table 1a. Hardening parameters for slip systems.

Parameter	Mg-0.9wt.%Zn-0.1wt.%Ca (ZX10) (M_{eff} = 0.2)			Mg-1.8wt.%Zn-0.2wt.%Ca (ZX20) (M_{eff} = 0.4)		
	<*a*> prism	<*a*> basal	<*c*+*a*> pyr I	<*a*> prism	<*a*> basal	<*c*+*a*> pyr I
τ_0^{α} (MPa)	36	9	85	35	15	230
k_1^{α} (m^{-1})	3.5×10^8	0.5×10^8	5.5×10^8	2.7×10^8	0.9×10^8	5.5×10^8
D^{α} (MPa)	50	50	50	50	50	50
g^{α}	2.5×10^{-3}	2.5×10^{-3}	3.0×10^{-3}	2.7×10^{-3}	9.0×10^{-3}	3.5×10^{-3}
q^{α}	4.0	4.0	4.0	4.0	4.0	4.0
HP^{α}	0.15	0.09	0.02	0.16	0.1	0.03

Table 1b. Hardening parameters for twinning.

Parameter	Mg-0.9wt.%Zn-0.1wt.%Ca (ZX10)	Mg-1.8wt.%Zn-0.2wt.%Ca (ZX20)
$\tau_0^{\beta}(\mathrm{MPa})$	18	21
$\mathrm{HP}^{\beta}(\mathrm{MPa})\sqrt{m}$	0.09	0.09
C^{β}	50	50

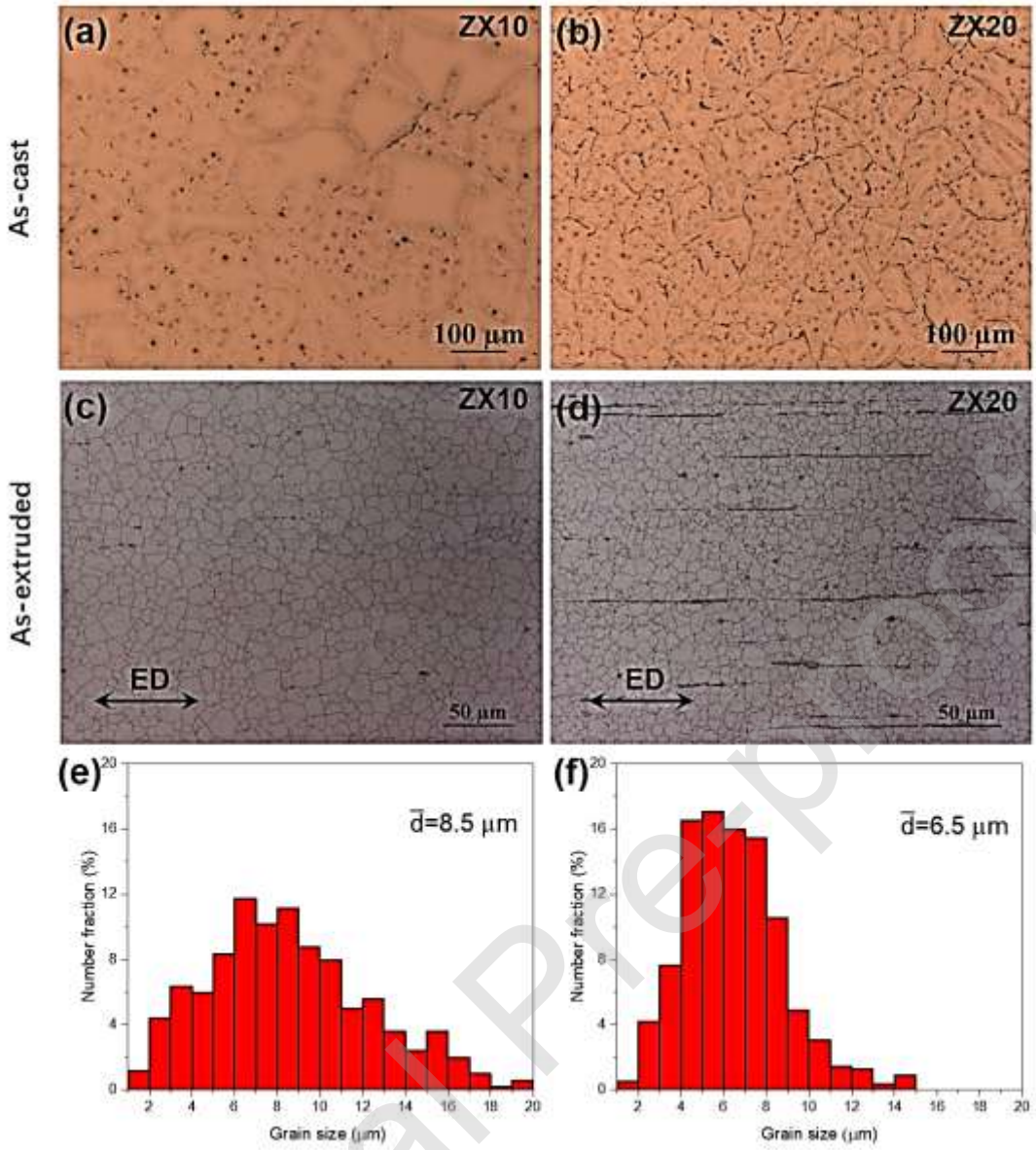

Fig. 1. Optical micrographs showing the initial microstructures of the two designed Mg-Zn-Ca alloys: (a, b) as-cast, (c,d) as-extruded. (e,f) the grain size distribution of the extruded alloys.

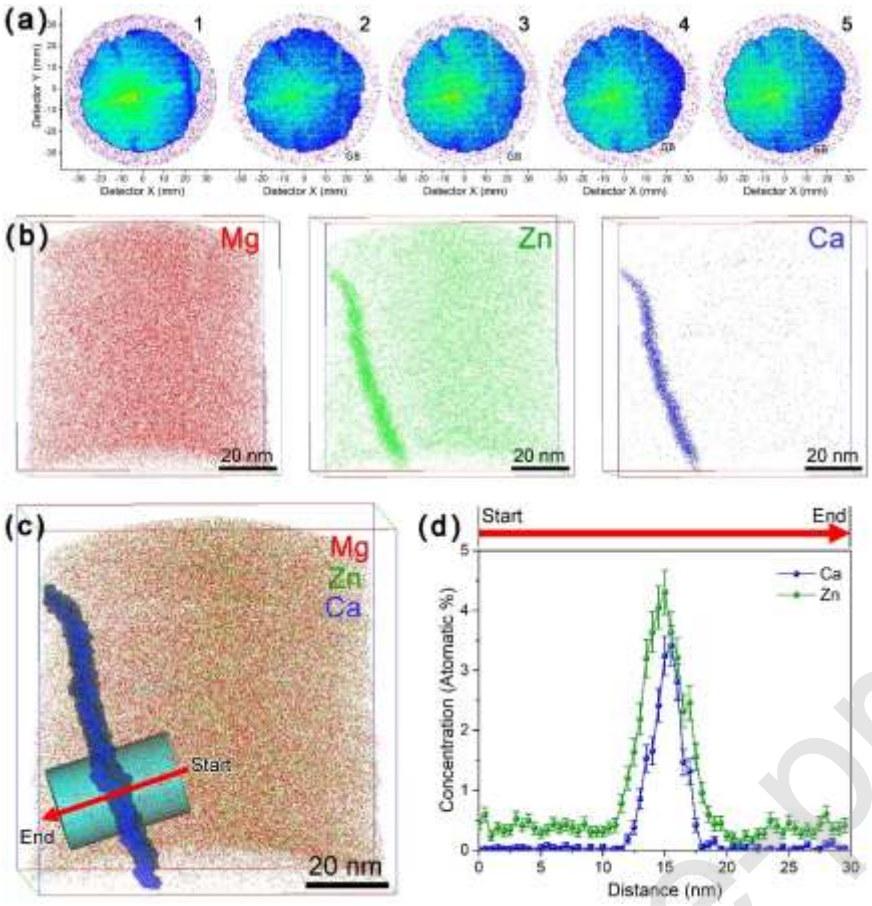

Fig. 2. Three-dimensional APT reconstruction of the extruded ZX20 local structure containing a grain boundary. (a) Mg atom density maps for the APT analysis volume calculated for different sections, showing two different poles, with grain boundary indicated by dotted lines. (b) Distributions of Mg, Zn, and Ca atoms in the sample. (c,d) Solute concentration profiles normal to the grain boundary from the APT analysis volume shown in (b).

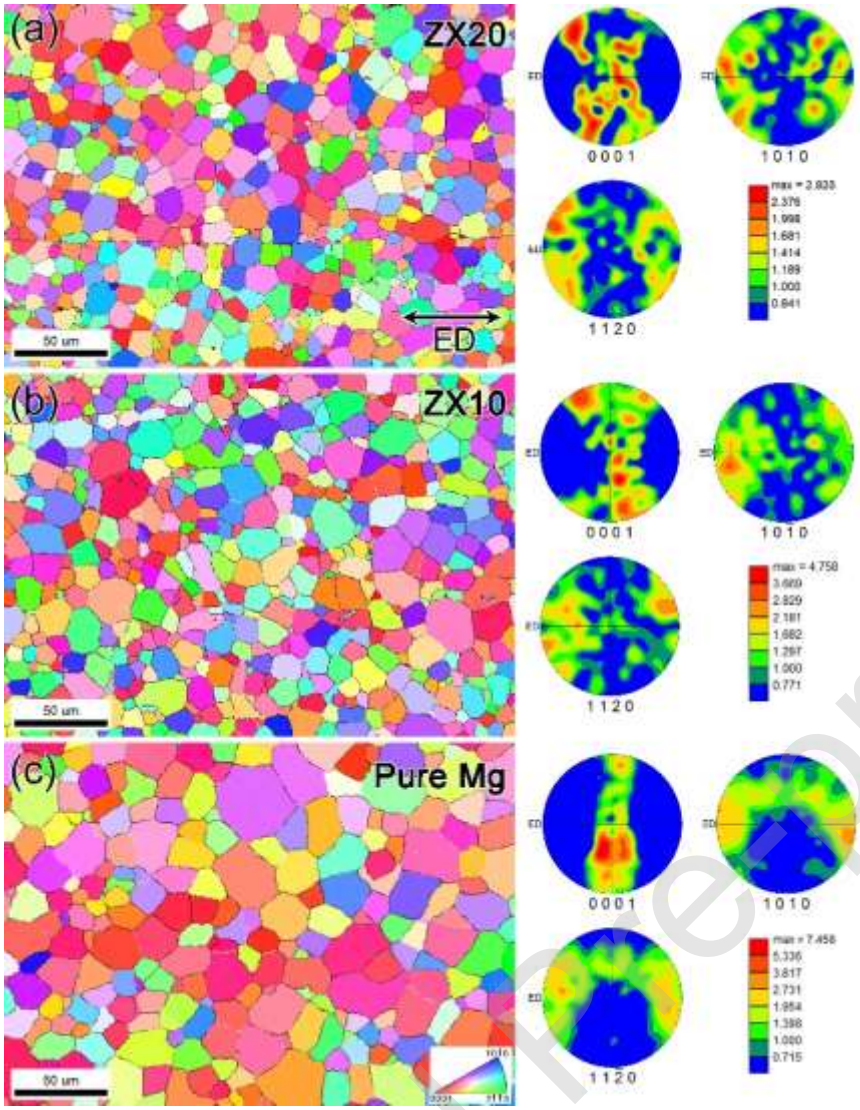

Fig. 3. Inverse pole figure (IPF) maps and pole figures (PF) of (a) ZX20, (b) ZX10, and (c) pure Mg. The colors in the IPF maps represent the grain orientations with respect to the TD.

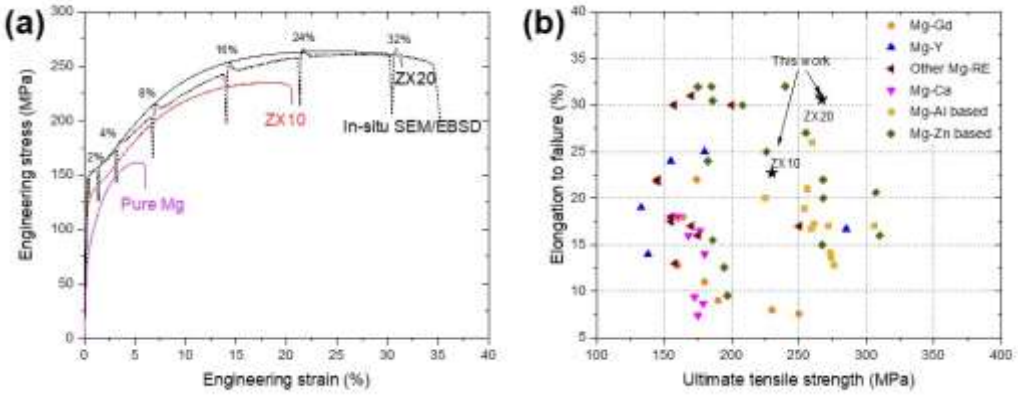

Fig. 4. (a) Tensile stress-strain curves along ED of ZX20, ZX10, and pure Mg. (b) Comparison of mechanical properties for the most commonly studied Mg alloys in Refs. [4,7–9,11,13–15,27–29,35,46,75]. Mg-Zn-Ca ternary alloys are included in the Mg-Zn based alloys in Fig. 4(b).

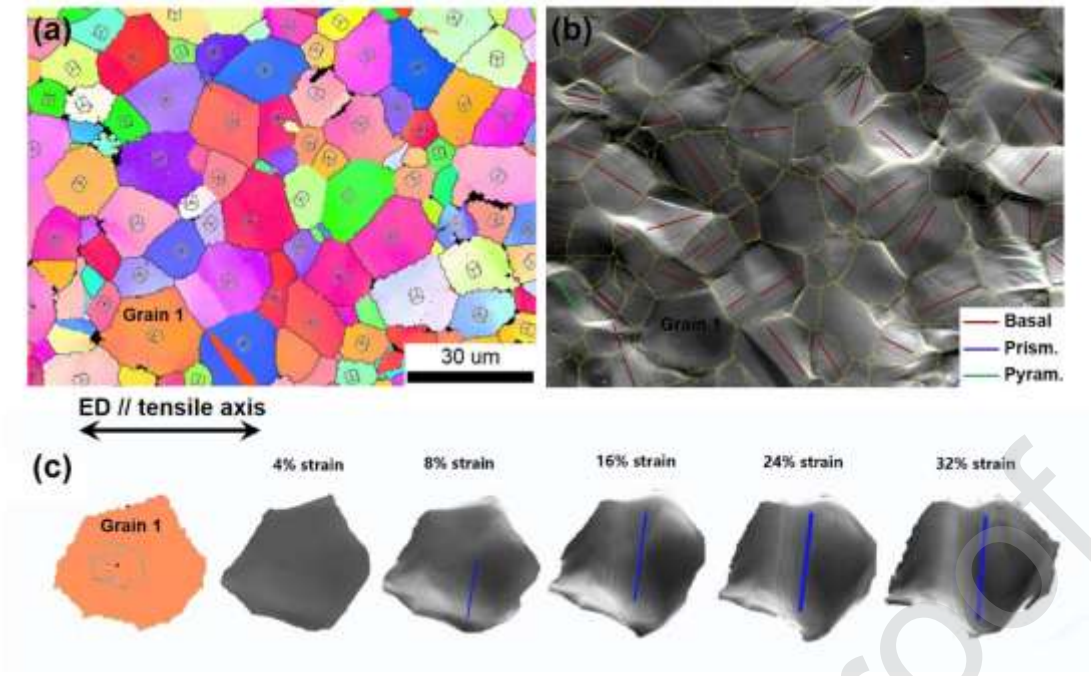

Fig. 5. (a) An EBSD map of ZX20 at 4% of tensile strain, showing absence of deformation twinning activity for majority of the grains. The grain orientations are represented by hexagonal unit cells. (b) Secondary electron image of the same area as in (a), showing the slip lines developed on the surface of the sample after 4% of tensile strain. (c) A selected grain developing prismatic slip lines after 8% of tensile strain.

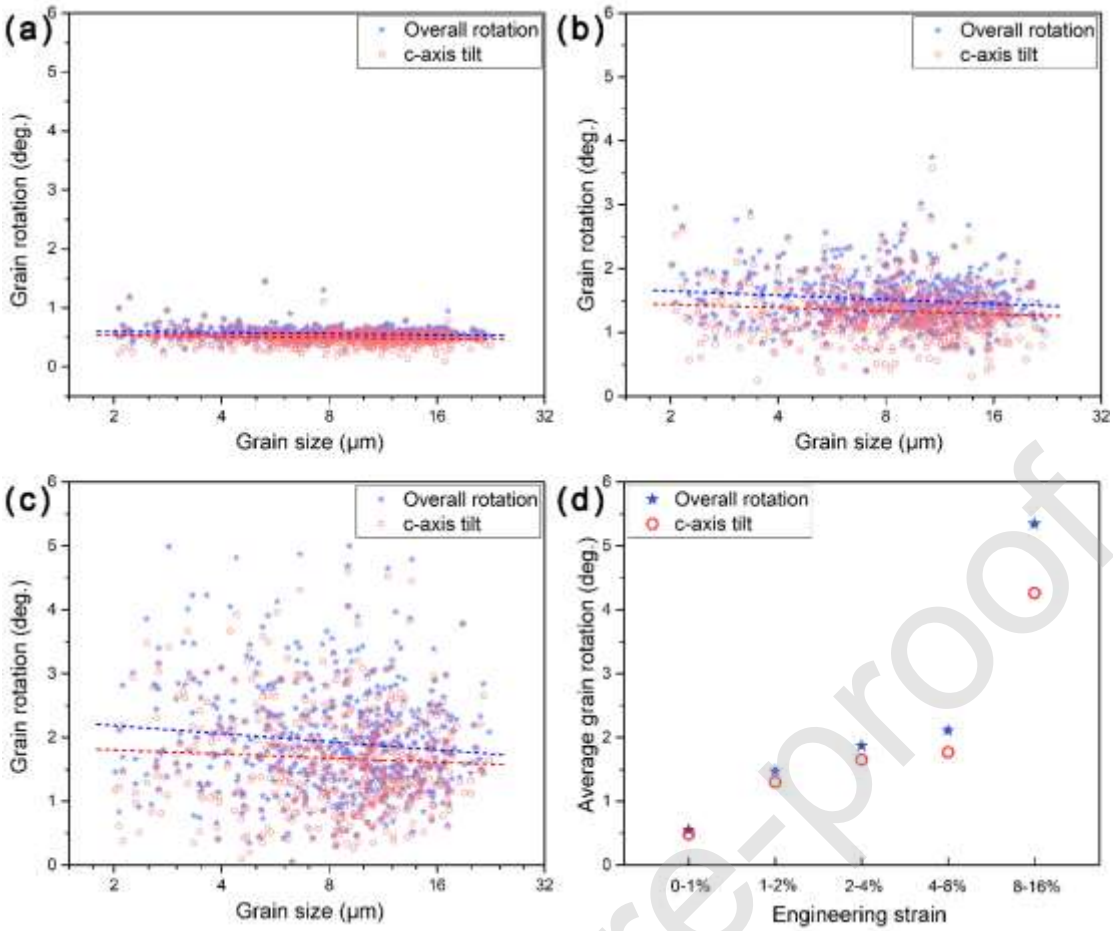

Fig. 6. Distribution of grain orientation rotation with respect to the grain size measured for: (a) 798 grains from 0% to 1% strain, (b) 749 grains from 1% to 2% strain, (c) 746 grains from 2% to 4% strain in ZX20 alloy during tension test. (d) Average amount of grain rotation and the *c*-axis tilt associated with the grain rotation as a function of engineering strain for ZX20 alloy.

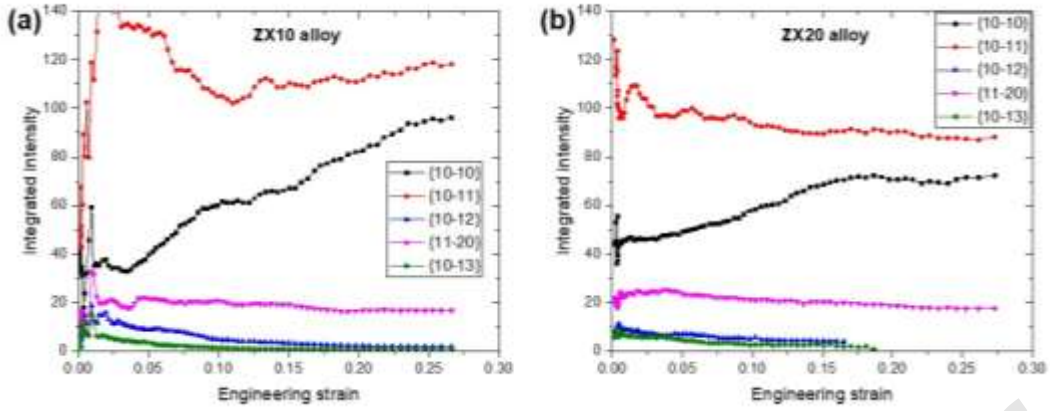

Fig. 7. Evolution of peak intensity for selected diffraction peaks as a function of engineering strain for ZX10 and ZX20.

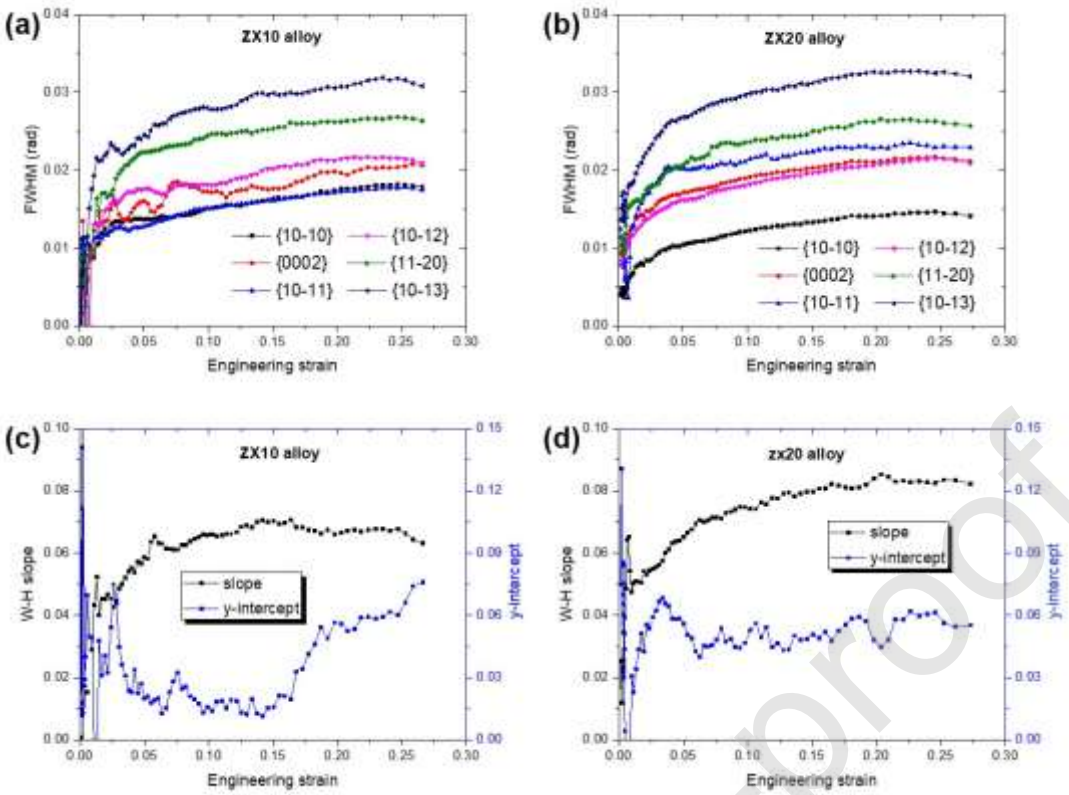

Fig. 8. Evolution of FWHM of different diffraction peaks as a function of engineering strain during tensile deformation (a, b), W-H slope and *y*-intercept as a function of engineering strain for ZX10 and ZX20 alloys (c, d).

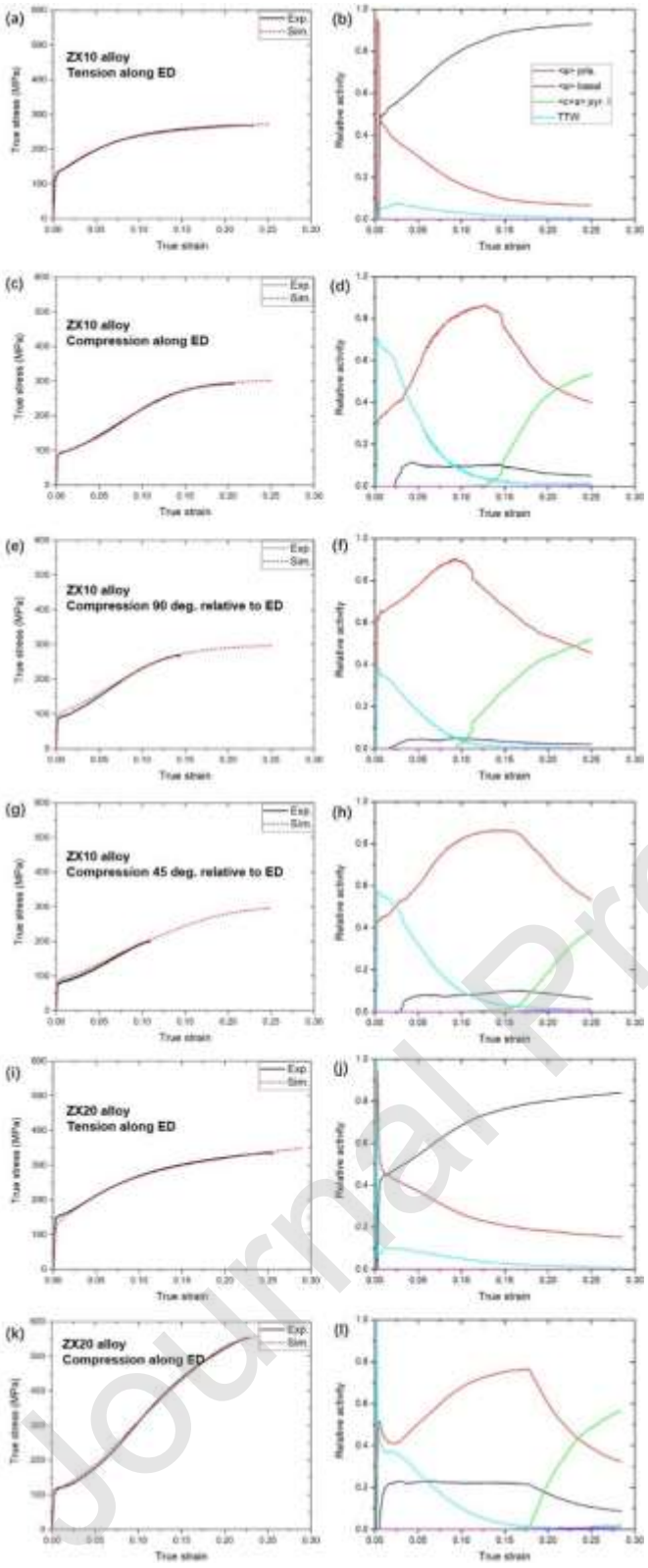

Fig. 9. Comparison of the experimental and simulated true stress-strain responses in simple tension and compression along with the directions as indicated in the figures along with predicted relative activities of each deformation mode.

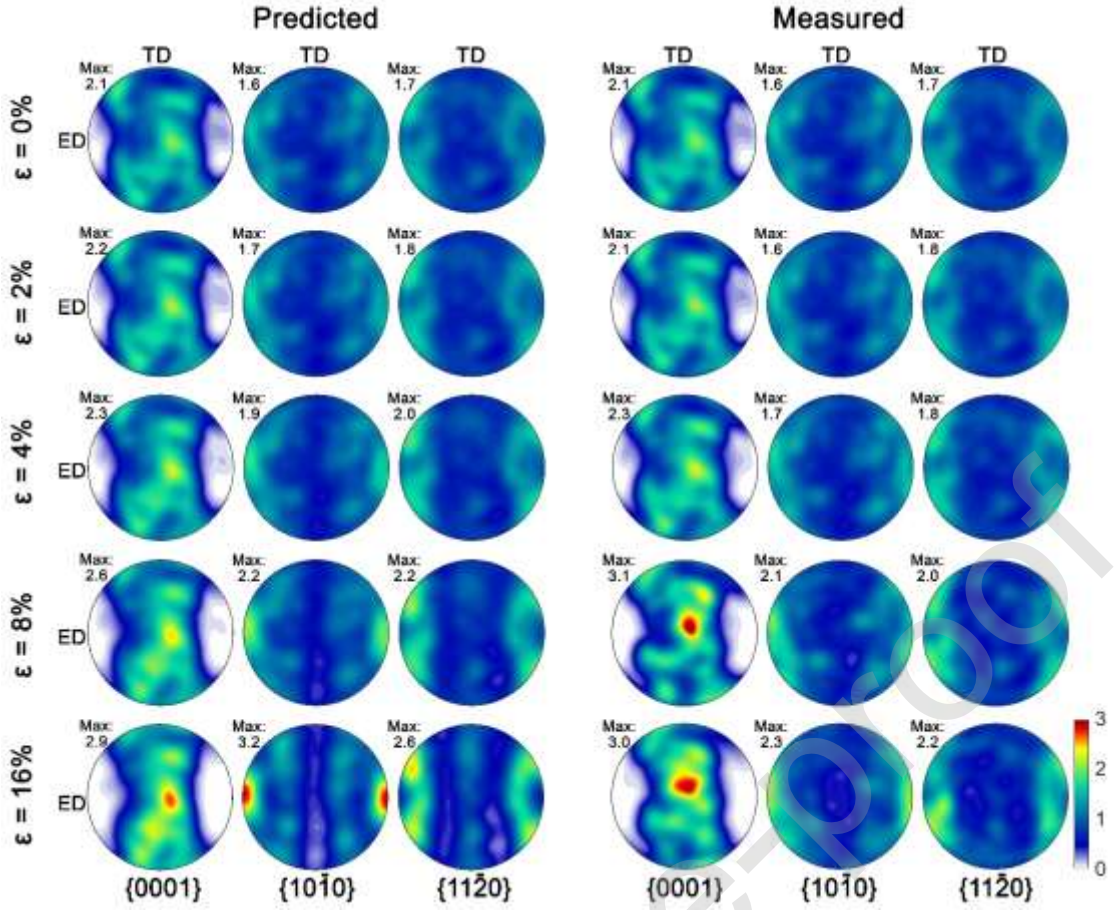

Fig. 10. Stereographic pole figures showing a comparison of the measured and predicted texture evolution of ZX20 alloy deformed in simple tension along with ED to certain strain levels.

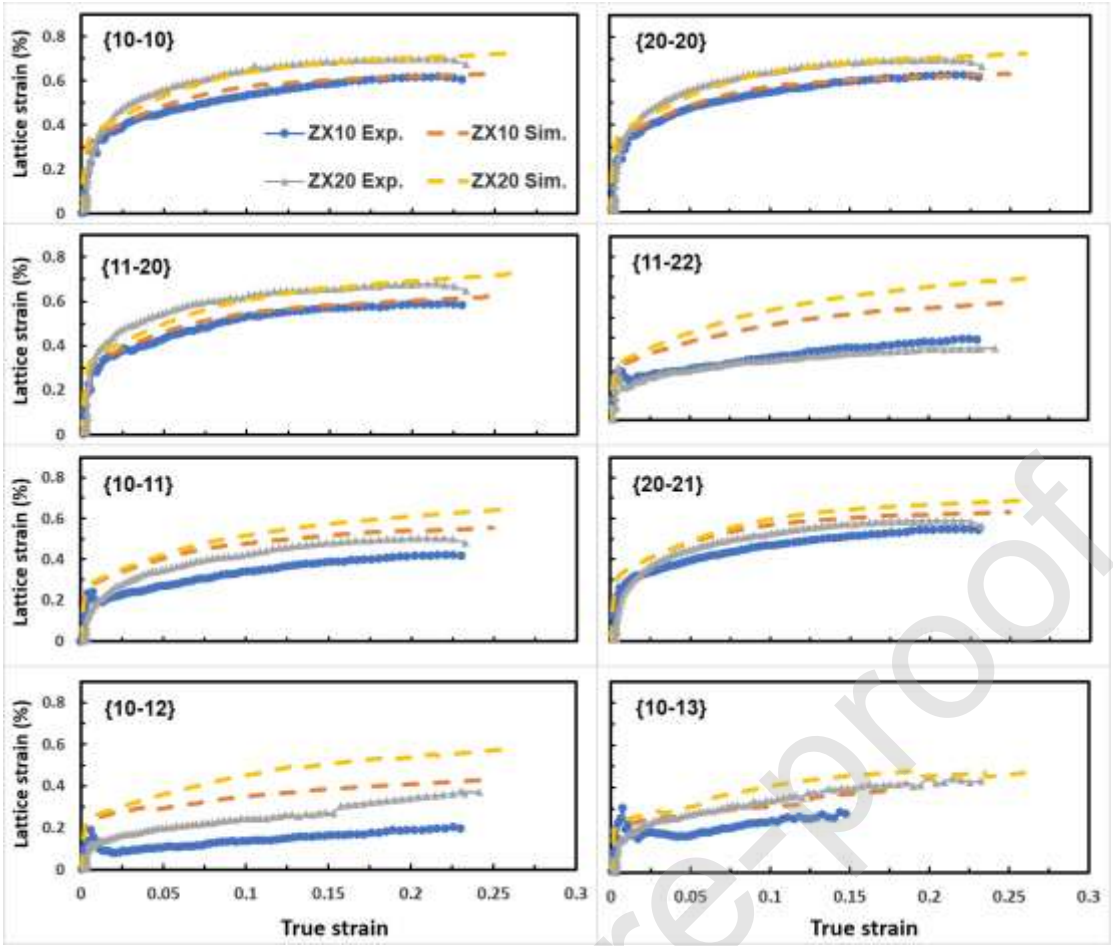

Fig. 11. Comparison of the experimental and simulated lattice strains for selected diffraction peaks.

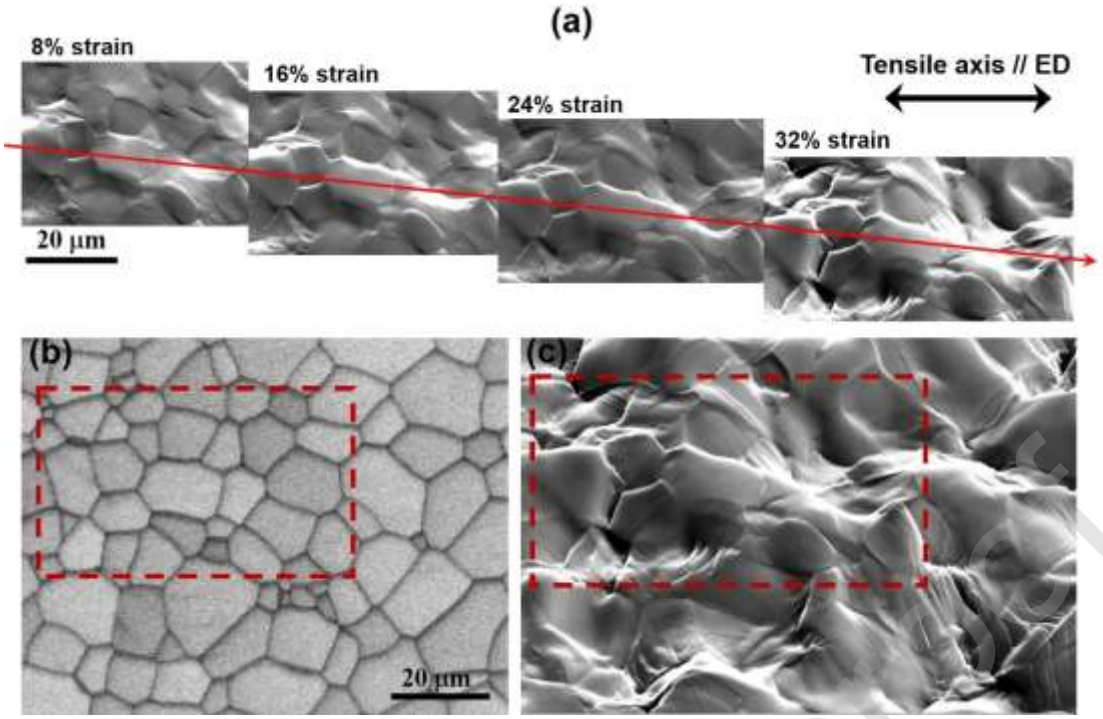

Fig. 12. (a) Secondary electron images of a selected area of ZX20 tensile specimen at different strains. (a) Image quality of ZX20 alloy showing the grain structure prior to deformation. (c) A magnified secondary electron image of ZX20 alloy at 32% tensile of strain. Dashed rectangles in both (b) and (c) show a same area as in (a).

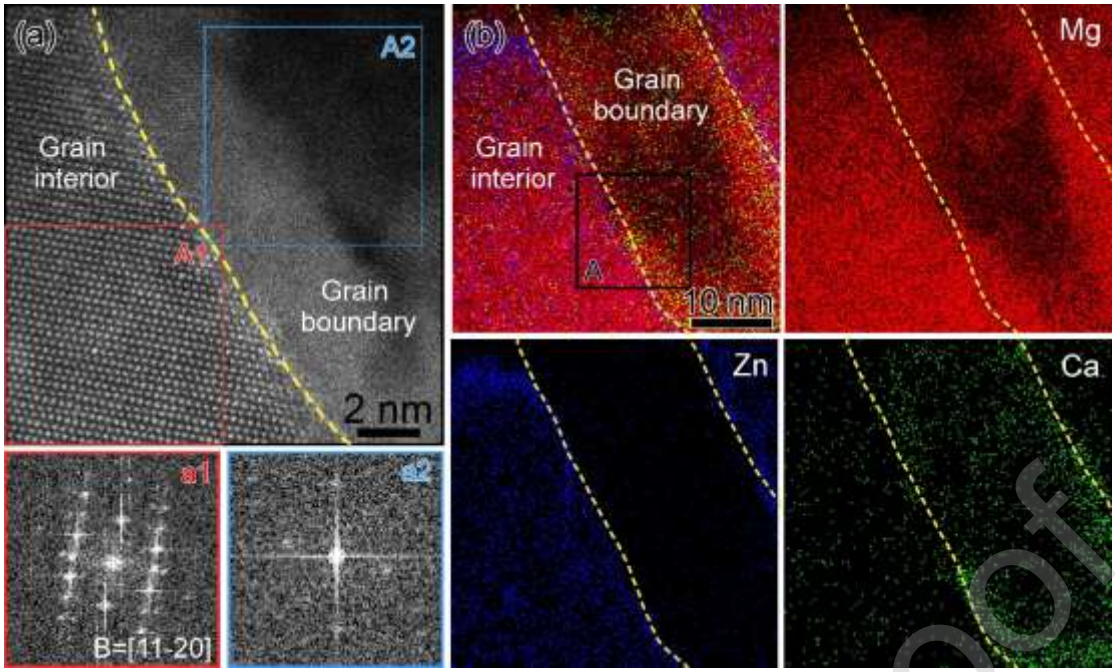

Fig. 13. (a) A HAADF-STEM image showing the microstructure of ZX20 alloy after tensile fracture, the fast Fourier transformation (FFT) patterns obtained from the grain interior and grain boundary are presented (marked as red square and light blue square respectively). (b) Elemental maps of Mg, Zn, and Ca obtained from the observation region containing the grain boundary as showed in (a).